Pergamon

Geochimica et Cosmochimica Acta, Vol. 67, No. 3, pp. 401–412, 2003

0016-7037/03 $22.00 + .00

PII S0016-7037(00)01081-5

Structural and compositional evolution of Cr/Fe solids after indirect chromate reduction by dissimilatory iron-reducing bacteria

C. M. HANSEL,[1,]* B. W. WIELINGA,[2] and SCOTT FENDORF[1]*

[1]Stanford University, Department of Geological and Environmental Sciences, Braun Hall, Bldg. 320, Room 118, Stanford, CA 94305, USA
[2]MFG, Inc., 3801 Automation Way, Suite 100, Fort Collins, CO 80525, USA

(*Received January* 23, 2002; *accepted in revised form July* 31, 2002)

Abstract—The mobility and toxicity of Cr within surface and subsurface environments is diminished by the reduction of Cr(VI) to Cr(III). The reduction of hexavalent chromium can proceed via chemical or biological means. Coupled processes may also occur including reduction via the production of microbial metabolites, including aqueous Fe(II). The ultimate pathway of Cr(VI) reduction will dictate the reaction products and hence the solubility of Cr(III). Here, we investigate the fate of Cr following a coupled biotic–abiotic reduction pathway of chromate under iron-reducing conditions. Dissimilatory bacterial reduction of two-line ferrihydrite indirectly stimulates reduction of Cr(VI) by producing aqueous Fe(II). The product of this reaction is a mixed Fe(III)-Cr(III) hydroxide of the general formula $Fe_{1-x}Cr_x(OH)_3 \cdot nH_2O$, having an α/β-FeOOH local order. As the reaction proceeds, Fe within the system is cycled (i.e., Fe(III) within the hydroxide reaction product is further reduced by dissimilatory iron-reducing bacteria to Fe(II) and available for continued Cr reduction) and the hydroxide products become enriched in Cr relative to Fe, ultimately approaching a pure $Cr(OH)_3 \cdot nH_2O$ phase. This Cr purification process appreciably increases the solubility of the hydroxide phases, although even the pure-phase chromium hydroxide is relatively insoluble. *Copyright © 2003 Elsevier Science Ltd*

1. INTRODUCTION

Industrial wastewater discharge, along with a suite of other anthropogenic activities, has lead to widespread Cr contamination within soils and water. Although Cr is an essential element for humans, the hexavalent form is toxic, mutagenic, and carcinogenic (National Research Council, 1974). As such, the widespread presence of Cr in the environment poses a serious threat to human and animal welfare. In the United States, Cr is the third most common pollutant at hazardous waste sites and is the second (after Pb) most common inorganic contaminant (National Research Council, 1991). The toxicity of Cr, however, is a function of oxidation state. In natural systems, Cr exists in two stable oxidation states, Cr(VI) and Cr(III). Hexavalent Cr, which typically exists as the oxyanion chromate (CrO_4^{2-}), has a high solubility in soils and groundwater and, as a consequence, tends to be mobile in the environment. In contrast, the reduced form of chromium, Cr(III), has a limited hydroxide solubility and forms strong complexes with soil minerals (Sass and Rai, 1987). Although trivalent Cr is relatively innocuous and immobile, hexavalent Cr is actively transported into cells by the sulfate transport system where it is capable of causing lesions in DNA as well as indirectly generating oxygen radicals (Bianchi and Levis, 1987). Accordingly, reduction of Cr(VI) to Cr(III) is considered an important remediation strategy for mitigating the deleterious effects of this toxin.

Methods for chromium remediation include excavation, pump and treat, in situ vitrification, and chemical treatment with a reductant (Vermeul et al., 1995). Bioremediation is currently receiving attention as an alternative remediation strategy supported by the discovery that some bacteria possess chromate reductase activity (Park et al., 2000). Within natural environments, however, the reduction pathway, and subsequent fate of Cr(VI), will be defined by the operating reaction kinetics of competing microbial and chemical reactions. Common chemical reductants of Cr(VI) include sulfides, dissolved organic compounds, aqueous Fe(II), and Fe(II)-bearing minerals (Pettine et al., 1994, 1998; Makos and Hrncir, 1995; Fendorf and Li, 1996; Patterson et al., 1997; Sedlak and Chan, 1997). Although cometabolic (and possibly metabolic) reduction of Cr(VI) by metal-reducing bacteria has been demonstrated (Lovley and Phillips, 1994; Tebo and Obraztsova, 1998; Francis et al., 2000; Fredrickson et al., 2000; Park et al., 2000), kinetic factors favor chemically induced reduction mechanisms within anaerobic environments. Even when considering maximum bacterial reduction rates, Fe(II) ($pH > 5.5$) and S(-II) ($pH < 5.5$) will dictate the fate of Cr(VI) within anaerobic soils (Fendorf et al., 2000). Consequently, within anaerobic soils, Fe(II) and sulfide will be the dominant mechanisms controlling the redox status of chromium with the predominant mechanism depending primarily on pH (Fendorf et al., 2000). Nevertheless, microbial activity will have an indirect bearing on Cr(VI) cycling because the generation of chemical reductants, for example, Fe(II), S(-II), is reliant upon microbial respiration of Fe(III) and sulfate. Reduction and subsequent immobilization of chromate may therefore result from a coupled biotic–abiotic reaction pathway in which $Fe(II)_{(aq)}$ or H_2S produced during microbial respiration catalyzes the reduction of Cr(VI) (Wielinga et al., 2001).

Reaction products following Cr(VI) reduction and their stability will depend on the specific mechanism by which reduction takes place; either direct enzymatic reduction or reaction with reduced metabolic products may occur. Although either pathway ultimately leads to metal reduction, the resulting prod-

---

* Authors to whom correspondence should be addressed (hansel@stanford.edu; fendorf@stanford.edu).

ucts and rate of reduction may differ appreciably. Correspondingly, the mechanism responsible for Cr(VI) reduction will dictate the solubility of the Cr(III) reaction product. For example, enzymatic reduction of chromate may result in soluble Cr(III) organic complexes that can be stable for extended periods of time (James and Bartlett, 1983), whereas, in contrast, reduction by Fe(II) and S(-II) results in insoluble $Cr_{1-x}Fe_x(OH)_3 \cdot nH_2O$ precipitates (Sass and Rai, 1987). Reduction by both Fe(II) and S(-II) will result in a precipitate with the general formula $Cr_{1-x},Fe_x(OH)_3 \cdot nH_2O$. Within pure systems, sulfide induced reductive precipitation will generate a solid with $x = 0$, and Fe(II) will give values of $x > 0$, specifically $x = 0.75$ (Eary and Rai, 1989; Patterson et al., 1997). The solubility of the Cr(III)-hydroxide precipitates is proportional to the ratio of Cr(III) to Fe(III), with increased quantities of Fe(III) stabilizing the solid (Sass and Rai, 1987). Accordingly, it is important to not only define the pathways for Cr(VI) reduction but also the resultant solids responsible for Cr(III) attenuation.

We have previously demonstrated sustained Cr(VI) reduction via a closely coupled, biotic–abiotic reductive pathway under iron-reducing conditions (Wielinga et al., 2001). Ferrous iron generated during dissimilatory Fe(III) reduction of ferric (hydr)oxides by *Shewanella alga* strain BrY serves as an effective reductant of Cr(VI) with a maximum sustainable Cr(VI) reduction rate of 5.5 $\mu g\ Cr^{VI} \cdot mg\text{-}cell^{-1} \cdot h^{-1}$. Iron (hydr)oxides of varying structures and stabilities ranging from ferrihydrite ($Fe(OH)_3 \cdot nH_2O$) to hematite ($\alpha\text{-}Fe_2O_3$) were investigated and revealed similar Fe(III), and hence Cr(VI), reduction rates. We also demonstrated that this reaction pathway is cyclic in nature, in that ferrous iron is oxidized back to the ferric state during Cr(VI) reduction. Systems varied in the degree of iron cycling and hence solid-phase composition. Accordingly, here we address the solid-phase properties of two systems, both having 2-line ferrihydrite as the electron acceptor that underwent different degrees of iron cycling. We elucidate the compositional evolution, speciation, and structural environment of Cr and Fe within the solid-phase products formed following this indirect Cr(VI) reduction pathway. We further address the consequences of Fe cycling on Cr(III) sequestration and solubility within these systems.

2. MATERIALS AND METHODS

2.1. Experimental Approach

We examined microbially induced ferrous iron-mediated reduction of Cr(VI) with *Shewanella alga* strain BrY (ATCC No. 51181, hereinafter referred to as BrY) as a model dissimilatory iron-reducing bacterium. BrY is a well-characterized, facultative anaerobic bacterium with a demonstrated ability to couple the oxidation of organic acids and H_2 to the reduction of Fe(III), Mn(IV), and U(VI) under anoxic conditions (Caccavo et al., 1992). Standard methods for culture of anaerobic bacteria and preparation of anoxic media were used throughout. Media and buffers were made anoxic by boiling and cooling under a stream of O_2-free N_2 or N_2:CO_2 (80:20) gas. All reactions were performed in an anaerobic chamber (Coy Laboratories, Grass Lake, MI) with an N_2 (90%):H_2(10%) atmosphere. BrY was grown aerobically to late log phase in tryptic soy broth (TSB; Difco, Detroit, MI) at 32°C and frozen back in 20% glycerol at −80°C. Seed cultures were started from frozen stocks (1 mL in 100 mL TSB) and grown aerobically for 8 h at 32°C (150 rpm). Cell suspensions were prepared by adding 1 mL of the seed culture to 100 mL of TSB and grown to late log phase (12 h, 32°C, 150 rpm). Cells were harvested by centrifugation (4500 *g* 10 min, 5°C), washed twice in 100 mL of anaerobic HEPES (30 mM; $C_8H_{18}N_2O_4S$) or bicarbonate buffer (2.5 g $NaHCO_3$ and 2.5 g NaCl per liter, pH 7.0), and resuspended in the same buffer. Cell suspensions were transferred to sterile, anaerobic pressure tubes with a headspace of N_2 gas, capped with a thick butyl rubber stopper, and stored on ice for less than 15 min before inoculation of flow cells.

Iron/chromium reduction reactions were performed in polycarbonate stirred-flow reactors (see fig. 2 in Wielinga et al., 2001) containing either 100 mL of either 30 mM HEPES or 10 mM sodium bicarbonate buffered medium, which also contained the following ingredients (g/L): NaCl, 2.5; NH_4Cl, 1.5; KCl, 0.1; $CaCl_2$, 0.1; $MgSO_4$, 0.1 mL vitamin and 10 mL mineral solutions (Balch et al., 1979). Lactate (as sodium lactate) was added as the electron donor to give a final concentration of 10 mM. Reduction experiments contained two-line ferrihydrite (nominally $Fe(OH)_3 \cdot nH_2O$) as the terminal electron acceptor (TEA). Ferrihydrite was synthesized by the titration of $Fe(NO_3)_3 \cdot 9H_2O$ (0.4 mol/L) with 1 mol/L NaOH to pH 7 (Ryden et al., 1987). The two-line ferrihydrite was washed with ultrapure water and maintained as an aqueous suspension. Ferrihydrite was added to provide a surface area of $\sim$10 m^2.

Reactions were initiated by adding cell suspension (final cell concentration $\sim 2 \times 10^7\ mL^{-1}$) and two-line ferrihydrite to each reactor and bringing the volume to approximately 100 mL with Cr-free medium. A 0.2-μm pore-size filter and filter-backing disk were placed on top of the chamber, and the reactor was sealed. The filter served to retain the cells and the iron solids in the reactor. Media was pumped into the bottom of the reactor, and effluent was forced out through the filter to the fraction collector. The initial flow rate before Cr addition varied between 10 and 11 mL/h. After Cr addition, the pump speed was adjusted downward until a steady-state Fe(II) concentration was maintained in the effluent. The flow rate varied from $\sim$1.5 to 3.5 mL/h. Samples collected were analyzed for soluble iron and chromium as described below.

Previously, we performed both negative and positive quality controls and investigated the ability for BrY to directly reduce Cr(VI) (Wielinga et al., 2001). The rate of Cr(VI) reduction by BrY was considerably slower than those observed for Cr(VI) reduction by Fe(II). Additionally, prolonged reduction of Cr(VI) by BrY was not observed, and reduction ceased after 20 h, perhaps as a result of Cr toxicity.

2.2. Solution Analysis

Production of soluble Fe(II) was monitored spectrophotometrically at 562 nm by means of the ferrozine method (Stookey, 1970). Dissolved Cr(VI) was measured spectrophotometrically at 540 nm by the s-diphenyl carbazide method (Bartlett and James, 1979). Total dissolved Cr and Fe were determined by flame atomic absorption spectroscopy or by inductively coupled plasma optical emission spectroscopy.

2.3. Solid-Phase Analysis

2.3.1. X-Ray Absorption Spectroscopy

We used both X-ray absorption near-edge structure (XANES) and extended X-ray absorption fine structure (EXAFS) spectroscopies to determine the speciation (oxidation states) and structural environment surrounding the absorbing atom (Cr or Fe). At the end of the experiments, solids within the suspension were dried in the anaerobic glovebox, mounted on a Teflon plate, and sealed with Kapton polymide film to prevent moisture loss and oxidation while minimizing X-ray adsorption. Solids remained in the glovebox until time of analysis. X-ray absorption spectroscopy (XAS) data were collected on beamlines IV-1 and IV-3 (beamline IV is an eight-pole wiggler) at the Stanford Synchrotron Radiation Laboratory, running under dedicated conditions. The ring operated at 3 GeV, with a current ranging from $\approx$100 mA to $\approx$50 mA. Energy selection was accomplished with a Si (220) monochromator typically with an unfocused beam. Higher-order harmonics were eliminated by detuning the monochromator $\sim$50% for Fe and 60% for Cr. Absorption spectra were recorded by monitoring the Cr K_α and Fe K_α fluorescence with a wide-angle ionization chamber (Lytle et al., 1984) for model compounds or a 13-element Ge semiconductor detector for unknown samples. A Mn (for Fe) and V (for Cr) filter along with Soller slits were used to minimize the effects of scattered primary radiation when the fluorescent ionization chamber is used. Incident and transmitted intensities were measured with in-line ionization chambers. The energy range studied was -200 to $+1000$ eV about the K_{α}-edge of Fe (7111 eV) and Cr (5989 eV). Each scan was calibrated internally by placing an elemental foil between the second and third in-line ionization chambers. Between 5 and 10 individual spectra were averaged for each sample. All spectra were collected at ambient temperature and pressure.

Spectra were analyzed by WinXAS and EXAFSPAK software (George, 1993; Ressler et al., 2000). Fluorescence spectra were background subtracted and the atomic absorption normalized to unity. Isolation of the EXAFS function [$\chi(k)$] was accomplished by fitting a spline function to the absorption envelope and then subtracting it from the spectra. The $\chi(k)k^3$ (where $k(\text{Å}^{-1})$ is the photoelectron wave vector) spectrum was Fourier-transformed to produce the radial structure function (RSF) in R-space (Å). Peaks in the Fourier transform were individually isolated and backtransformed (Fourier filtered). A nonlinear least-squares procedure was used to fit both the Fourier-filtered and raw spectra by use of theoretical reference XAS phase-shift and amplitude functions. Phase-shift and amplitude functions for both single- and multiple-scattering (MS) paths were generated with the ab initio computer code FEFF 7 (Rehr et al., 1991, 1992) by using atomic clusters from well-characterized crystalline model compounds. The theoretical FEFF functions were initially fit to experimental XAS data of reference compounds to determine values for σ^2 and to estimate errors in fitting. Bond lengths were accurate within ±0.04 Å and coordination numbers within ±20% for first through third shells. Experimental unknown spectra were then fit using the theoretical phase and amplitude functions and the coordination number (N), interatomic distance (R), and disorder (σ^2) were varied to optimize the goodness of fit (F) or minimize the residual (R). Values for E_0 were determined from first-shell fits and were subsequently fixed in fits to higher-shell backscatterers. As explained in O'Day et al. (1994), the contribution of MS paths to the EXAFS spectra was investigated by identifying potential MS paths in FEFF 7 and then comparing the amplitude of each path (estimated by an approximate plane-wave calculation) to that of the path with the largest amplitude and including potential MS paths in experimental fits.

A set of reference standards for Fe were utilized to perform linear combination k^3-weighted EXAFS spectra fitting by the EXAFSPAK module DATFIT (George, 1993). Linear fitting routines were used to reconstruct the unknown to determine the relative percentages of mineral phases within the samples. Linear combinations of empirical model spectra were optimized, where the only adjustable parameters were the fractions of each model compound contributing to the fit. Fits were optimized by minimizing the residual of the fit, defined as the normalized root square difference between the data and the fit. Accuracy of linear combination analysis was investigated by fitting a set of mixed standards having known fractions. Fits were within ±7% of the actual percentages.

Model Fe compounds used in FEFF calculations and DATFIT linear combinations include siderite ($FeCO_3$), ferrihydrite ($Fe(OH)_3 \cdot nH_2O$), goethite (α-FeOOH), lepidocrocite (γ-FeOOH), hematite (α-Fe_2O_3), green rust ($Fe^{II}_{6-x}Fe^{III}_{x}(OH)_{12}[(SO_4)_{x/2} \cdot 3H_2O]$), vivianite ($Fe_3(PO_4)_2 \cdot nH_2O$), and magnetite ($Fe_3O_4$). Siderite, vivianite, and magnetite were natural samples obtained from the Stanford University Mineral Collection. Goethite, hematite, ferrihydrite, and lepidocrocite were synthesized following the procedures of Schwertmann and Cornell (2000) and green rust following Schwertmann and Fechter (1994). Synthesized standards were verified via powder X-ray diffraction analysis.

Model Cr compounds used include chromite ($FeCr_2O_4$), Cr(III) hydroxide, and mixed Fe(III), Cr(III) hydroxides ($Fe_{1-x}Cr_x(OH)_3$; x ranges from 0.75 to 0.25). Chromite was obtained from the Stanford Mineral Collection. Chromium hydroxide was synthesized by titrating 20 mM $CrCl_3$ to pH 6; pH was maintained at this value for 24 h (Fendorf et al., 1994). The synthesized chromium hydroxide possesses a γ-CrOOH local structure as observed previously (Charlet and Manceau, 1992; Fendorf et al., 1994). The $Fe_{1-x}Cr_x(OH)_3$ standards were synthesized by titrating stoichiometric concentrations of $Fe(NO_3)_3$ and $CrCl_3$ solutions with 0.1 mol/L NaOH to pH 7 and pH was maintained for 3 d. Ratios of Fe(III):Cr(III) within the solids were verified with X-ray wavelength dispersive spectroscopy (JEOL JXA-733A Superprobe). Quantitative analysis of samples was performed by the CITZAF matrix correction algorithm. Background correction was obtained by using the mean atomic number method and standards were analyzed before and after sample analysis to account for drift. Comparative results indicate an error for major elements of less than 1% and less than 5% for minor elements. Analyses were performed in triplicate and good agreement between the predicted and observed ratios were observed (Table 1).

Table 1. Ratios of mixed Fe and Cr hydroxides.

	Mole fraction Cr(III)[a]		
Cr(III):Fe(III)	Predicted	Observed[b]	Solid formula
1:3	0.25	0.24 ± 0.003	$Fe_{0.75}Cr_{0.25}(OH)_3$
1:2	0.33	0.33 ± 0.004	$Fe_{0.67}Cr_{0.33}(OH)_3$
1:1	0.50	0.50 ± 0.004	$Fe_{0.50}Cr_{0.50}(OH)_3$
2:1	0.67	0.66 ± 0.003	$Fe_{0.33}Cr_{0.67}(OH)_3$
3:1	0.75	0.75 ± 0.001	$Fe_{0.25}Cr_{0.75}(OH)_3$

[a] Cr(III)/(Fe(III) + Cr(III)).

[b] Value represented as mean with ± first standard deviation $\sqrt{(n\Sigma x^2 - (\Sigma x)^2)/(n(n-1))}$

2.3.2. *Microscopy*

Scanning electron microscopy was utilized to determine mineral morphologies. At the termination of the experiments, solids within the suspension were dispersed onto carbon-coated Al mounts and allowed to dry in the glovebox. Samples were coated with Au and examined with a JEOL JSM-5600LV scanning electron microscope equipped with backscatter and secondary electron detectors and an energy dispersive X-ray analytical system.

3. RESULTS AND DISCUSSION

3.1. Reaction Progression: Solution Chemistry

Previously, we demonstrated the reduction of Cr(VI) via Fe(II) produced during iron respiration by using four structurally diverse ferric (hydr)oxides (α-Fe_2O_3, α-FeOOH, 2- and 6-line ferrihydrite) (Wielinga et al., 2001); data for two-line ferrihydrite as the terminal electron acceptor are provided in Figure 1a. Differences in sustained reduction are evident between the HEPES-buffered (FC8) vs. bicarbonate-buffered (FC10) systems. Although reduction ceased after 76 h in the bicarbonate-buffered systems, reduction continued unabated in the HEPES-buffered systems until it was intentionally terminated at 168 h. This discrepancy may arise from the complexation of Fe(II) and, particularly, Cr(III) in the presence of HEPES, thus delaying sorption and potential poisoning of the hydroxide and/or cell surface. As illustrated previously, removal of potential sorbates via complexation allows for enhanced iron reduction (Urrutia et al., 1999). Although all of the Cr entering the bicarbonate-buffered systems is retained in the solid-phase, merely 45% is retained in the presence of HEPES (Fig. 1b). Within both systems, however, no Cr(VI) is detected in the effluent suggesting that Cr(III) is being complexed and eluted from the HEPES-buffered system. Although thermodynamic data were not available for HEPES complexes with Cr(III) or Fe(III), we have observed substantial complexation of Fe(III) and Cr(III) by HEPES in independent laboratory experiments, supporting our contentions here.

Considering the initial Fe(III) provided (as two-line ferrihydrite) and the reduction rate, reduction should be maintain for

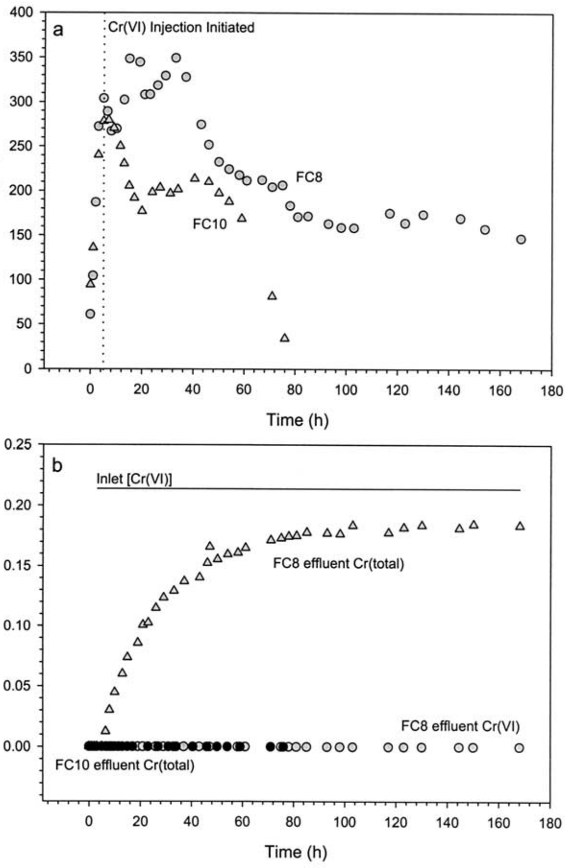

Fig. 1. Comparison of temporal changes in (a) effluent aqueous Fe(II) concentration for ferrihydrite reduction by BrY and (b) subsequent Cr chemistry within HEPES (FC8) and bicarbonate buffered (FC10) media. Dotted line represents time at which continuous Cr(VI) injection was initiated.

only ~70 h. Thus, for Fe(III) reduction to continue beyond 70 h, Fe within the system must be (re)cycled back to the ferric state—a redox cycle between the bacteria and chromate must be established. Correspondingly, the two systems represent differing degrees of iron cycling. Iron is cycled approximately twice in FC8 (HEPES) and once in FC10 (bicarbonate). The following discussion focuses on the solid-phase transformations within these two systems and the potential consequences of Fe cycling on mineral structure and stability.

3.2. Iron Solid-Phase Characterization

3.2.1. *Oxidation State*

XANES spectra were utilized to determine the oxidation state of Fe within the solid-phase products. Consistent with previous studies, normalized absorption and first-derivative XANES spectra of Fe minerals illustrate a 2- to 4-eV energy shift associated with a one-unit valence difference (Fig. 2) (Waychunas et al., 1983; Kemner et al., 2001). The XANES spectra of solid-phase products from FC8 and FC10 reveal a predominance of Fe(III) in an oxo or hydroxyl coordination environment (Fig. 2). The absorption edge-crest (~7128 eV) and inflection point (noted by the peak in the first-derivative spectra at ~7124 eV) correspond to that of ferric iron within both samples; thus, if ferrous iron is present in the sample, it accounts for less than 5% (detection limit) of total Fe.

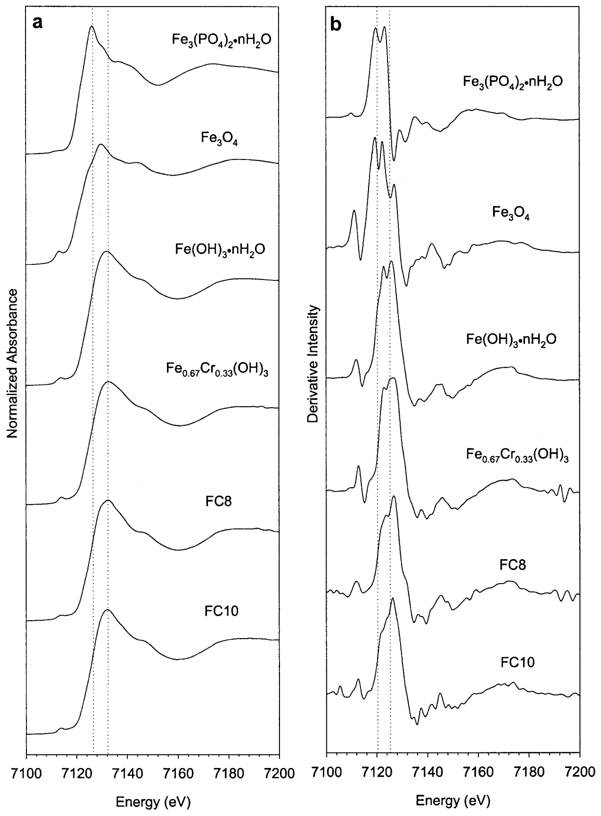

Fig. 2. Iron (a) X-ray absorption spectra and (b) first-derivative XANES spectra of model compounds and Fe associated with the solid-phase biomineralization products FC8 (cycled) and FC10 (not cycled). Model compounds ferrihydrite (ferric), magnetite (ferric–ferrous), and vivianite (ferrous) were included to illustrate the relative energy shifts. Only oxygen coordinated Fe minerals were included to eliminate effects (effective charge) of different ligands (Waychunas et al., 1983). Dashed lines refer to energy positions for ferrous (lower energy) and ferric (higher energy) iron.

3.2.2. *Structural Environment*

Previous studies illustrate the sensitivity of EXAFS spectroscopy to changes in the short-range structure of Fe (hydr)oxides (Manceau and Combes, 1988; Manceau and Drits, 1993). A topological approach for polyhedral frameworks was previously applied to discern the local structure of Fe(III) within solids that was based on EXAFS spectra. This approach interprets the local order of a metal (hydr)oxide on the basis of a correspondence between metal-metal distances and the polyhedral linkages in the (hydr)oxides. The four Fe (hydr)oxide octahedral linkages encountered are face (F, 2.89 Å), edge (E, 2.97 to 3.34 Å), double-corner (DC, 3.37 to 3.51 Å), and single-corner (SC, 3.87 Å). The local order of Fe hydroxides (e.g., α-Fe_2O_3, $\alpha/\beta/\gamma$-FeOOH) can be classified on the basis of the number and type of aforementioned octahedral linkages. However, it is important to note that this approach assumes that the metal-metal distances depend mainly on the nature of the octahedral linkages and that the correspondence between linkage and bond distance remains valid in the absence of long-range order, for example, ferrihydrite (Combes et al., 1989). We use this approach in the following structural investigations of the solid-phase products of the two aforementioned systems varying in their degree of Fe cycling. Subsequently, structural analysis is focused on radial distance determination (constraining Debye-Waller factors to realistic values on the basis of reference compounds) and less emphasis is applied to coordination number.

The Fourier-filtered EXAFS spectra and corresponding RSFs of four Fe (hydr)oxide standards, two mixed Fe, Cr hydroxide standards, and bioreduction products (FC8 and FC10) are illustrated in Figure 3. Distinct structural features among the phases are more easily observed in the Fourier-filtered EXAFS function; thus, both the filtered (Fig. 3) and raw spectra of the unknowns (Fig. 4) are depicted (fitting parameters were equivalent between the two). Parameters derived from optimal fits to the raw spectra are presented in Table 2. Structural variations within the EXAFS spectra of the four Fe (hydr)oxides are manifested in the ~4 to 5.5 and >9.5 Å^{-1} ranges (Fig. 3). Moreover, the location and intensity of the oscillation at ~7.5 Å^{-1} varies considerably among the four (hydr)oxides. Comparison of the spectral line shape suggests that the mixed Fe, Cr hydroxides and FC10 adopt a ferrihydrite-like structure. FC8, however, appears to have structural features common to both ferrihydrite and hematite (additional oscillation at ~5.1Å^{-1}).

The local coordination environment of Fe within ferrihydrite, α-FeOOH, γ-FeOOH, α-Fe_2O_3 are consistent with previous distances (Manceau and Combes, 1988; Manceau and Drits, 1993). However, resolution of the individual shells within the Fourier-transform is limited by the extent of the data in the reciprocal space (k), where $k_{\max} \geq \pi/2\Delta R$. For consistency among spectra, all Fe spectra were truncated at 11.5 Å^{-1} allowing for a distance resolution of ~0.14 Å within the Fourier-transform. Thus, Fe-Fe atomic shells at 3.28 to 3.34 and 3.46 to 3.51 Å are difficult to resolve (Manceau and Drits, 1993). Accordingly, although α-FeOOH has two edge-sharing octahedra at 3.01 Å and 3.28 Å and 4 double-corner sharing octahedra at 3.46 Å, only two contributing shells (3.03 and 3.43 Å) are observed with the k-range used here (Table 2). Thus, distinguishing between β-FeOOH (2 at 3.03, 2 at 3.34, and 4 at 3.51 Å) and α-FeOOH is difficult (Combes et al., 1989; Charlet and Manceau, 1992; Manceau and Drits, 1993). For the purposes of this study their distinction is not of concern and hence the two will be considered collectively as α/β-FeOOH.

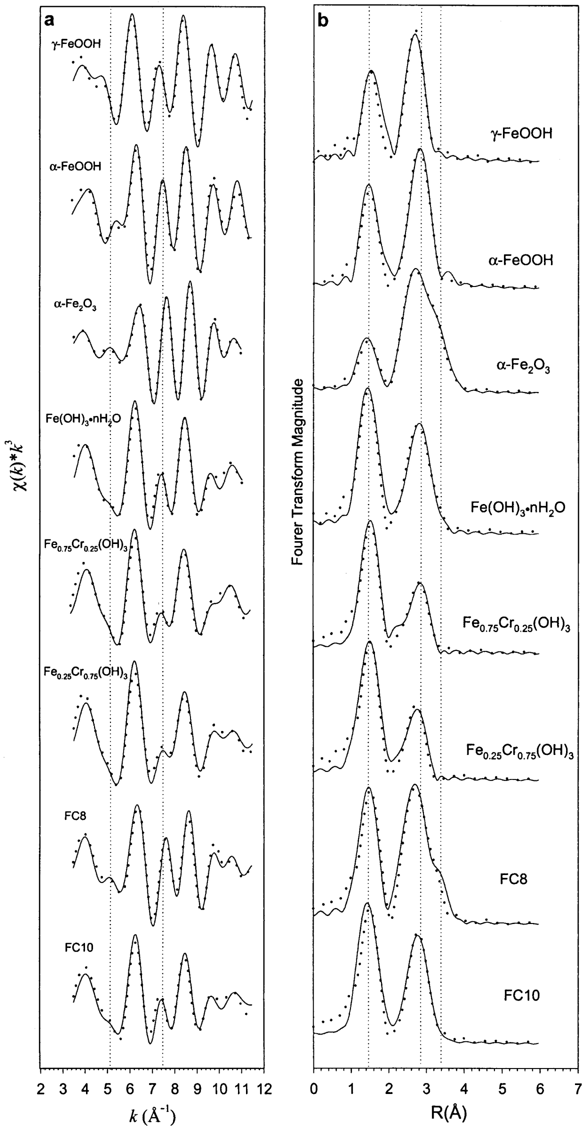

Fig. 3. Iron (a) Fourier-filtered (first two shells, R = ~0.9 to 3.2 (3.7) Å) EXAFS spectra and corresponding (b) Fourier transforms for Fe standards and unknowns, FC8 (cycled) and FC10 (not cycled). All EXAFS and RSF data (solid line) were fit (dotted line) over k = 3 to 11.5 Å^{-1} for consistency as a result of noise at high k region in some spectra. Only the two end members of the mixed Fe, Cr hydroxides are presented because of the equivalence of the spectra throughout the solid-solution series.

Structural parameters for ferrihydrite indicate that it has principally an α/β-FeOOH local structure (Table 2). Although not evident as a result of the resolution imposed within this study, the local structure of ferrihydrite is intermediate between that of α-Fe_2O_3 and α/β-FeOOH (Manceau and Drits, 1993). Similarly, the Fe-Fe(Cr) distances for $Fe_{0.75}Cr_{0.25}(OH)_3 \cdot nH_2O$ and $Fe_{0.25}Cr_{0.75}(OH)_3 \cdot nH_2O$ correspond with α/β-FeOOH. Considering the similarity of the EXAFS spectral line shape between ferrihydrite and $Fe_{1-x}Cr_x(OH)_3 \cdot nH_2O$, it appears that the structural environment of Fe within the mixed hydroxides has a α/β-FeOOH local order, similar to that of ferrihydrite. Likewise, an Fe-rich end member ($Fe_{0.99}Cr_{0.01}(OH)_3 \cdot nH_2O$) was previously found to have an α-FeOOH local order (Charlet and Manceau, 1992). Although the structure of FC10 coincides with ferrihydrite, FC8 has an additional Fe-Fe(Cr) distance at 2.95 Å corresponding to an α-Fe_2O_3 contribution (Table 2). Inclusion of an Fe-Fe(Cr) contribution at 2.95 Å greatly enhances the least-squares fit to the experimental spectra ($\Delta F = 50$). This distance reflects the weighted average of one face-sharing octahedra at 2.89 Å and three edge-sharing octahedra at 2.97 Å within the α-Fe_2O_3 local structure. Thus, FC10 has a ferrihydrite structure and FC8 appears to be a composite of α-Fe_2O_3 and ferrihydrite.

Comparison of the Fourier transforms further demonstrates a spectral similarity between α-Fe_2O_3 and FC8 (Fig. 3). Although the other (hydr)oxides contain a single Fe-Fe(Cr) shell,

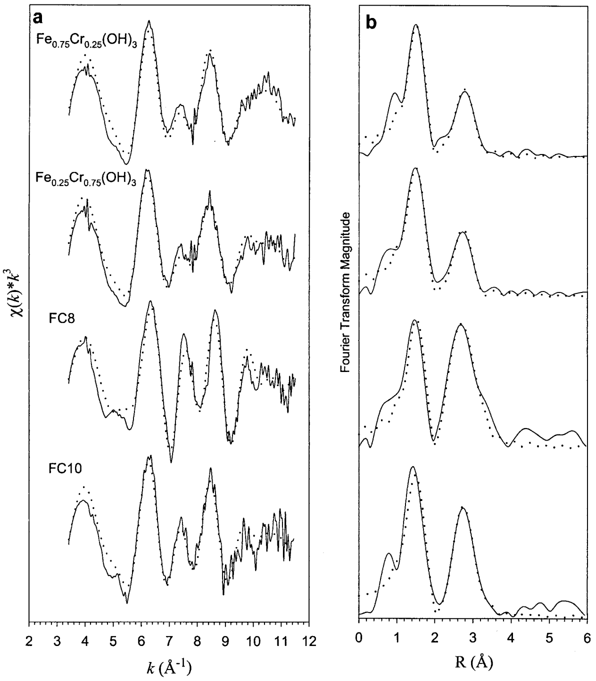

Fig. 4. Least-squares fits (dotted lines) to normalized k^3-weighted Fe EXAFS spectra (solid lines) for the biomineralization products FC8 (cycled) and FC10 (not cycled), and two end members of the mixed Fe, Cr hydroxide standards.

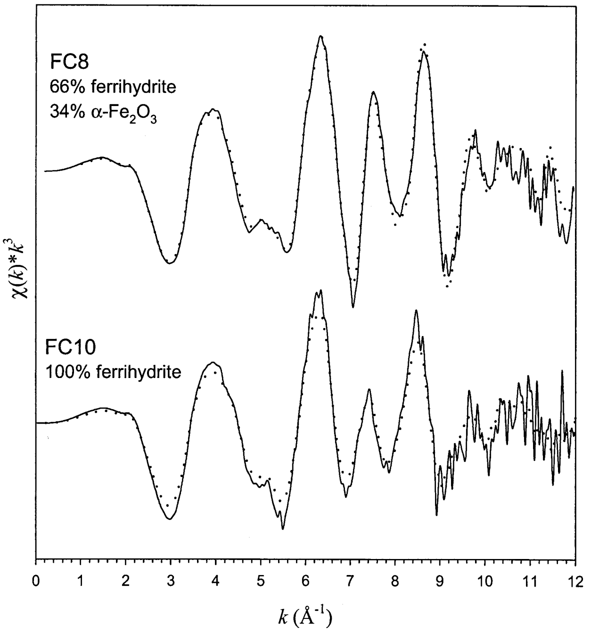

Fig. 5. Fe K-EXAFS spectra of FC8 (cycled) and FC10 (not cycled). Linear combination fits of model (dotted) and experimental spectra (solid) are overlain.

both FC8 and α-Fe_2O_3 contain an additional shoulder on this peak. For all spectra, the presence of only a single Fe-Fe(Cr) peak is a result of having a shortened *k*window and subsequent lower resolution for individual RSF peaks. However, although a larger *k*window allows for resolution of individual peaks within the RSF, distances obtained from structural fitting of the EXAFS spectra are equivalent (data not shown; discussed below for Cr).

Linear combination fitting of k^3-weighted EXAFS spectra further supports the aforementioned findings (Fig. 5). The solid-phase Fe EXAFS spectra from FC10 can be adequately reconstructed by the ferrihydrite spectra. Conversely, the optimized fit to the FC8 spectra consists of 66±7% ferrihydrite and 34±7% α-Fe_2O_3. It is interesting to note that $FeCO_3$ was not detected as a substantial product even within systems containing as high as 20 mM bicarbonate. Siderite rhombs were not observed after microscopic analysis, supporting the EXAFS analysis. As such, Fe(II) generated within the system that is not oxidized during chromate reduction is either lost from the system or adsorbed to the bacterial/hydroxide surface (i.e., no other Fe(II) mineral species are present).

We predicted previously that the solid-phase products would be poorly crystalline, thus providing the bacteria with a desir-

Table 2. Structural parameters derived from least-squares fits to raw, k^3-weighted Fe EXAFS spectra of model compounds and biomineralization products FC8 (cycled) and FC10 (not cycled).[a]

	Fe-O			Edge/face: Fe-Fe(Cr)			Corner: Fe-Fe(Cr)			
Element	r(Å)	N	σ^2	r(Å)	N	σ^2	r(Å)	N	σ^2	F
Lepidocrocite	1.99 (2)	5.5 (6)	0.008 (4)	3.08 (2)	4.8 (2)	0.005 (2)				45
Goethite	2.00 (2)	4.8 (2)	0.008 (7)	3.02 (4)	1.9 (2)	0.007 (4)	3.43 (2)	3.5 (3)	0.009 (1)	16
Ferrihydrite	2.00 (2)	4.8 (5)	0.007 (2)	3.02 (3)	2.0 (9)	0.008 (3)	3.43 (4)	3.5 (2)	0.009 (4)	11
Hematite	1.99 (2)	4.9 (1)	0.013 (2)	2.95 (2)	3.9 (1)	0.008 (2)	3.36 (3)	2.8 (2)	0.005 (4)	12
							3.69 (6)	4.9 (2)	0.009 (7)	
$Fe_{0.75}Cr_{0.25}(OH)_3 \cdot nH_2O$	2.00 (2)	4.9 (1)	0.015 (5)	3.03 (3)	1.9 (2)	0.014 (8)	3.42 (3)	3.2 (2)	0.010 (4)	44
$Fe_{0.25}Cr_{0.75}(OH)_3 \cdot nH_2O$	2.00 (3)	5.4 (2)	0.009 (5)	3.02 (3)	1.8 (3)	0.011 (8)	3.42 (6)	3.5 (3)	0.010 (7)	60
FC8	2.00 (1)	4.9 (1)	0.008 (2)	2.95 (2)	3.2 (2)	0.008 (1)	3.43 (5)	4.0 (2)	0.012 (6)	117
				3.02 (4)	1.7 (2)	0.010 (4)				
FC10	2.00 (3)	5.4 (2)	0.012 (4)	3.01 (3)	1.7 (2)	0.009 (4)	3.42 (1)	4.0 (1)	0.011 (2)	107

[a] Coordination number (N), interatomic distance (r), and Debye-Waller factor (σ^2) obtained from fitting raw data with theoretical phase and amplitude functions. F is the goodness of fit $= \Sigma[\chi(k)^2_{expt} - \chi(k)^2_{fit}]$. Fits were performed over the k range: 3 to 11.5 Å^{-1}. Distances reported in the table differ from those in the RDF because the latter were not corrected for phase shift. Estimated errors at 96% confidence interval from the least-squares fit are given in parentheses.

able, high surface area metabolic substrate (Wielinga et al., 2001). The results described above support this prediction, in that the solid-phase products in FC10 have a ferrihydrite-like structure. Upon further Fe cycling (FC8), however, the remaining Fe(III) progresses toward an α-Fe_2O_3-type structure. Ferrihydrite, being a metastable phase, transforms to more stable Fe (hydr)oxides (e.g., α-FeOOH, α-Fe_2O_3) over time (Cornell and Schwertmann, 1996). Although ferrihydrite has structural domains of both α-Fe_2O_3 and α/β-FeOOH, the mechanism of transformation to the products is quite different. Although α-Fe_2O_3 is considered a solid-state conversion of ferrihydrite, α/β-FeOOH is formed via dissolution/reprecipitation (Fischer and Schwertmann, 1975; Schwertmann and Murad, 1983; Manceau and Drits, 1993; Cornell and Schwertmann, 1996). The presence of face-sharing octahedra within ferrihydrite is thought to reduce the activation energy barrier needed for the conversion to α-Fe_2O_3, thus favoring its formation over α/β-FeOOH (Combes et al., 1990; Manceau and Drits, 1993). This mechanism is induced by dehydration and dehydroxylation of Fe-OH-Fe bonds resulting in an increase in the density of face linkages (Manceau and Drits, 1993). Conversion of ferrihydrite to α-FeOOH is also thought to be promoted by divalent metal (e.g., Fe(II)) sorption; thus, the short residence time of ferrous iron, the result of reoxidation by Cr(VI), may also inhibit the conversion of ferrihydrite to α/β-FeOOH (Cornell, 1988; Zachara et al., 2002). Accordingly, within the solid-phase products of FC8 and FC10, Fe is originally in a ferrihydrite-like structure, whereas the fraction of α-Fe_2O_3 within the solid grows at the expense of ferrihydrite over time. After two Fe cycles, the percentage of α-Fe_2O_3 within the solid-phase Fe is ~34%.

3.3. Chromium Solid-Phase Characterization

3.3.1. Oxidation State

Because of site symmetry differences between Cr(VI) and Cr(III), the preedge feature of the XAS spectra is utilized to determine the contribution of the two species (see, e.g., Patterson et al., 1997; Peterson et al., 1997). The preedge is caused by a bound-state 1s to 3d transition. Although this transition is allowed for noncentrosymmetric tetrahedral $Cr(VI)O_4$ molecules (as a result of 3d-2p orbital mixing), it is forbidden for octahedral $Cr(III)O_6$ having a center of symmetry. Additionally, the empty d-orbital ($3d^0$) in Cr(VI) increases the probability of this transition, thus enhancing the pre-edge peak intensity. Normalized absorption spectra of FC8 and FC10 reveal an absence of an appreciable contribution of Cr(VI) within the samples (Fig. 6). Similar to Fe, the absorption spectra reveal a prevalence of Cr(III) in an oxo or hydroxyl coordination environment. Considering that Cr(VI) was not detected in the effluent, all Cr(VI) entering the system is thus being reduced to Cr(III).

3.3.2. Structural Environment

The same approach as that used for the Fe analysis is used to interpret the Cr XAS data for FC8 and FC10. Normalized k^3-weighted EXAFS spectra for $Fe_{1-x}Cr_x(OH)_3 \cdot nH_2O$ standards (x ranges from 0.25 to 0.75) and corresponding FTs are illustrated in Figure 7. Structural parameters for least-squares fits to the experimental spectra are reported in Table 3. Similar to Fe, the short-range order of the mixed Cr, Fe hydroxides correspond with an α/β-MeOOH-like structure (Me = Cr or Fe) (Table 3). In contrast to Fe, however, the edge-sharing contribution at ~3.28 Å is included in the fitting parameters (Fig. 8). This result is in good agreement with a previous study indicating that during coprecipitation with Fe, Cr (as $Fe_{0.99}Cr_{0.01}(OH)_3$) is integrated into a hydrous ferric oxide (HFO) matrix having an α-type local structure (with two nearest-neighbor metal shells at 3.00 to 3.05 and 3.40 to 3.45 Å) (Charlet and Manceau, 1992). As discussed by Charlet and Manceau (1992), this phase is in structural discontinuity with homogenously precipitated Cr(III) hydroxide having a γ-CrOOH structure (two metal shells at 3.00 to 3.05 and 3.94 to 4.03 Å).

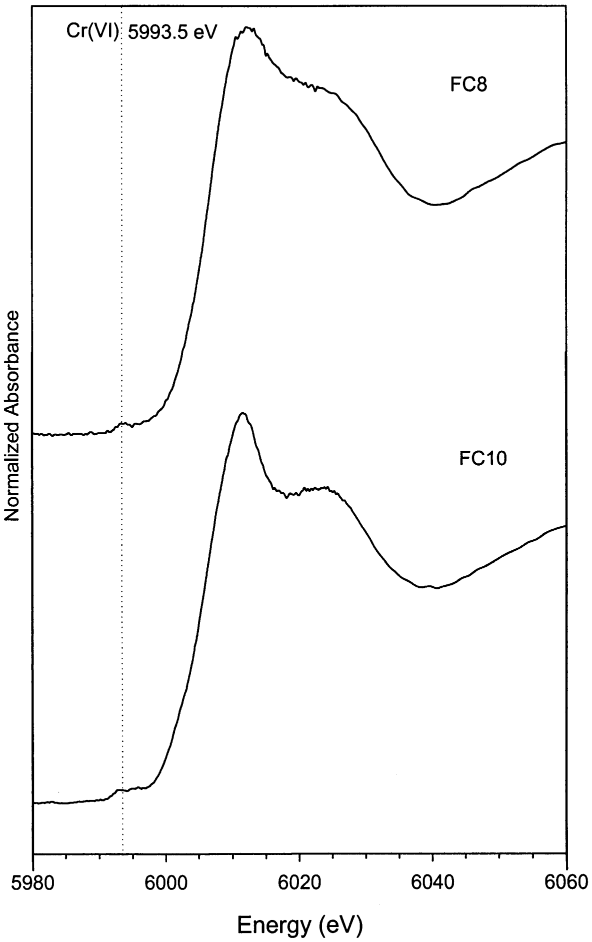

Fig. 6. Chromium X-ray absorption spectra windowed to illustrate the preedge region (~5993.5 eV) for the biomineralization products FC8 (cycled) and FC10 (not cycled).

Although the Fe-rich end member corresponds to an α-MeOOH-like structure, Cr-Fe(Cr) bond distances increase as the mole fraction of Cr within the solid increases. The bond distances for both edge-sharing octahedra within the solid undergo expansion from 3.04 Å and 3.26 Å to 3.06 Å and 3.30 Å, respectively. More salient, however, is the increase in the radial distance of the double-corner sharing peak from 3.48 to

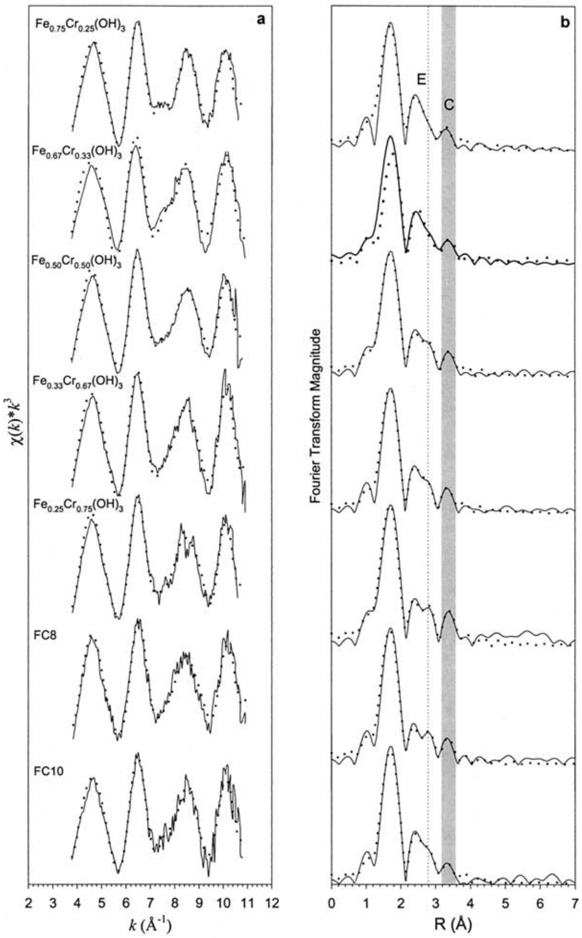

Fig. 7. Chromium (a) k^3-weighted EXAFS spectra and (b) corresponding Fourier transforms for Cr standards and unknowns, FC8 (cycled) and FC10 (not cycled). All data (solid line) were fit (dotted line) over $k = 3$ to 10.5 Å^{-1} for consistency as a result of noise at high k region in some spectra. Edge- (E) and corner-sharing (C) contributions are indicated.

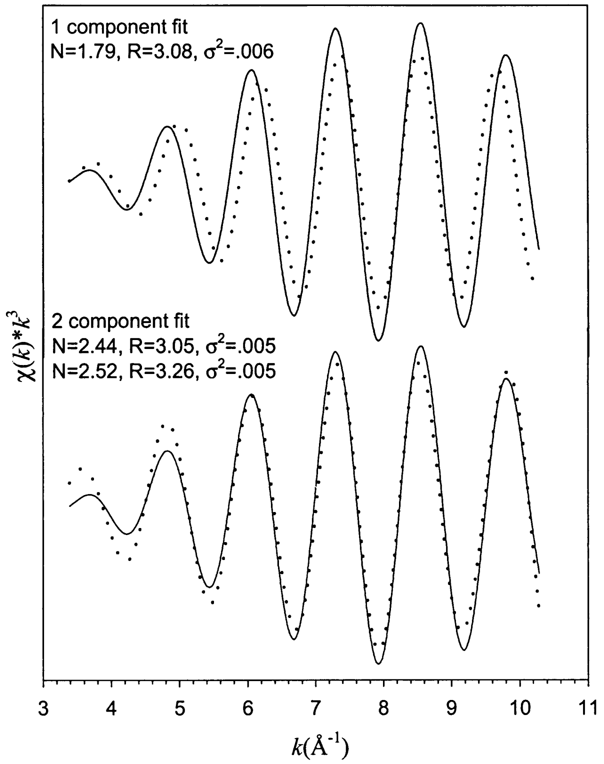

Fig. 8. Fourier-filtered Cr-Cr(Fe) contributions to EXAFS for $Fe_{0.67}Cr_{0.33}(OH)_3 \cdot nH_2O$ (solid line) and fits (dotted lines). Spectra are windowed to include Cr-Cr(Fe) peak from R = 2.07 to 2.98 Å.

3.56 Å as the mole fraction of Cr within the solid increases. This phenomena may be a result of structural expansion and octahedral rotation within the solid. Rotation of the double corner-sharing octahedra would result in said Cr-Fe(Cr) radial distances. This structural expansion/rotation appears to be a transitory feature, intermediate to the α/β-FeOOH structure of ferrihydrite and the γ-CrOOH structure of Cr hydroxide. Similarly, Cr(III) appears to prefer a corner-sharing arrangement as demonstrated by a γ-CrOOH local structure (Charlet and Manceau, 1992; Fendorf et al., 1994).

The spatial orientation and distribution of Fe/Cr atoms within this phase are unknown and merit further investigation. However, as aforementioned, the local order of Fe within $Fe_{1-x}Cr_x(OH)_3 \cdot nH_2O$ has an α/β-FeOOH structure, consistent with that of Cr. Conversely, Fe does not undergo structural expansion/rotation (corner-sharing distance remains ~3.44 Å), thus suggesting that Cr may exist in multiple domains within the solid, including a solid-solution with Fe having an α/β-CrOOH local structure and another, possibly, moving toward a γ-CrOOH structure. Consequently, it is possible that we are observing mixed α- and γ-MeOOH local structures. Similarly, Cr(III) sorbed to goethite is initially present as surface clusters having both α- and γ-MeOOH local environments but tends toward an exclusively γ-CrOOH environment at higher surface coverages (Charlet and Manceau, 1992). Nevertheless, although we do not observe Cr distances at 3.94 to 4.03 Å, it is important to note that we are obtaining an "average" of the local environment surrounding Cr. Iron adopts, in addition to α/β-FeOOH, an α-Fe_2O_3 local order, which Cr does not. This suggests that Fe may also exist in multiple, either spatially differentiated or intergrown, structural, domains within the solid-phase products. The compositional (Cr to Fe ratios), and hence structural heterogeneity, of the solids was confirmed by microscopic analysis.

3.3.3. *Ratio of Cr to Fe in the Solid Phase*

Of particular interest is the systematic enhancement of the Cr corner-sharing peak at 3.48 to 3.56 Å as the ratio of Cr to Fe in the hydroxide increases. The increase in the corner-sharing peak, normalized to the first Cr-Cr(Fe) shell, has a linear ($R^2 = 0.90$) relationship with the mole fraction of Cr(III) within the solid (Fig. 9a). By use of measured peak intensities, we determined the relative mole fraction of Cr(III) within the solid-phases from FC8 and FC10. Solid-phases produced via the reduction of Cr(VI) by Fe(II) are predicted to have a Cr:Fe of 1:3 illustrated by the following reaction:

Table 3. Structural parameters derived from least-squares fits to raw, k^3-weighted Cr EXAFS spectra of $Fe_{1-x}Cr_x$ hydroxides and biomineralization products FC8 (cycled) and FC10 (not cycled).[a]

	Cr-O			Edge: Cr-Cr(Fe)			Corner: Cr-Cr(Fe)			
Element	r(Å)	N	σ^2	r(Å)	N	σ^2	r(Å)	N	σ^2	R
$Fe_{0.75}Cr_{0.25}(OH)_3 \cdot nH_2O$	2.01 (2)	5.3 (1)	0.007 (3)	3.04 (4) 3.26 (1)	2.5 (2) 2.5 (3)	0.005 (4) 0.005 (5)	3.48 (2)	3.6 (3)	0.009 (4)	16
$Fe_{0.67}Cr_{0.33}(OH)_3 \cdot nH_2O$	2.01 (2)	5.0 (2)	0.006 (4)	3.05 (2) 3.26 (2)	2.4 (2) 2.5 (3)	0.005 (7) 0.005 (8)	3.51 (3)	3.8 (3)	0.009 (1)	26
$Fe_{0.5}Cr_{0.5}(OH)_3 \cdot nH_2O$	2.01 (2)	5.1 (2)	0.007 (3)	3.06 (4) 3.29 (6)	2.0 (2) 1.9 (3)	0.006 (5) 0.006 (3)	3.54 (8)	4.1 (3)	0.009 (6)	15
$Fe_{0.33}Cr_{0.67}(OH)_3 \cdot nH_2O$	2.01 (2)	5.7 (1)	0.007 (3)	3.06 (4) 3.29 (4)	2.0 (2) 1.8 (3)	0.006 (4) 0.006 (4)	3.54 (6)	4.2 (2)	0.009 (7)	20
$Fe_{0.25}Cr_{0.75}(OH)_3 \cdot nH_2O$	2.01 (2)	5.4 (2)	0.007 (3)	3.06 (4) 3.30 (5)	2.0 (2) 2.0 (2)	0.006 (5) 0.006 (4)	3.56 (7)	4.2 (3)	0.009 (6)	22
FC8	2.01 (2)	4.6 (1)	0.007 (3)	3.05 (7) 3.28 (6)	1.7 (2) 1.6 (3)	0.007 (6) 0.006 (5)	3.55 (1)	4.4 (3)	0.009 (2)	19
FC10	2.01 (2)	5.7 (1)	0.006 (2)	3.04 (4) 3.26 (4)	2.5 (2) 2.4 (3)	0.005 (4) 0.005 (5)	3.49 (6)	3.6 (3)	0.009 (8)	21

[a] Coordination number (N), interatomic distance (r), and Debye-Waller factor (σ^2) obtained from fitting raw data with theoretical phase and amplitude functions. R is the residual between the experimental and fitted spectra = $(\Sigma|\chi(k)^2_{\text{expt}} - \chi(k)^2_{\text{fit}}|)/(\Sigma|\chi(k)^2_{\text{expt}}|) \times 100$. Fits were performed over the k range: 3.6 to 10.8 Å^{-1}. Distances reported in the table differ from those in the RDF because the latter were not corrected for phase shift. Estimated errors at 96% confidence interval from the least-squares fit are given in parentheses.

$$3Fe^{2+} + HCrO_4^- + 8H_2O \rightarrow 4Cr_{0.25}Fe_{0.75}(OH)_3 + 5H^+ \tag{1}$$

Although solids from FC10 have an approximate Cr to Fe ratio of 1:2.5 ($Fe_{0.72}Cr_{0.28}(OH)_3 \cdot nH_2O$), FC8 mirrors that of FC10 with a ratio of 2.5:1 ($Fe_{0.29}Cr_{0.71}(OH)_3 \cdot nH_2O$). Solids from FC8 are enriched in Cr(III) relative to the predicted ratio suggesting that microbial reduction of Fe(III) within the solid is occurring. Both scanning electron microscopy and microprobe analysis further confirms the increase in the ratio of Cr to Fe within the solids over time.

Two distinctions exist between the FC8 and FC10 systems: duration of reduction and buffering agent. We propose that the enrichment of Cr(III) within FC8 relative to FC10 is a consequence of Fe cycling within the system. Considering that the HEPES buffered system (FC8) lost ~50% of the introduced Cr and merely 20% of Fe, then Fe should be enriched in the solids relative to Cr. Conversely, no Cr was detected in the effluent within the bicarbonate buffered system (FC10). However, whereas FC10 cycled through the original available Fe(III) once, FC8 cycled twice. These findings suggest that Fe(III) within the mixed hydroxides is available for further microbial respiration and that continued reduction results in the enrichment of Cr within the solids. Furthermore, as Fe(III) is cycled some solids will become purified with respect to Cr while fresh $Fe_{0.75}Cr_{0.25}(OH)_3 \cdot nH_2O$ solids precipitate.

3.3.4. *Consideration of Spectral Range and MS Paths*

As discussed previously for Fe, the effects of a shortened k window on the results of the least-squares fitting of the EXAFS spectra were investigated with the solid-phase products from FC10 (usable k window to 13.9 Å^{-1}) (Table 4). Bond distances were within 0.02 Å among the two windows and coordination numbers varied <10%. Nevertheless, for the purposes of this study, the results are sufficient to determine the local structure transformations within the solid-phase precipitates. However, it is important to note that coordination numbers for both Cr and Fe may be less accurate than those obtained with longer k ranges.

The contribution of MS paths to the EXAFS spectra was investigated from theoretical FEFF calculations. Within the radial distances of these phases, MS paths were for the most part less than 10% of the amplitude predicted for the first-shell backscatterers. Two potential exceptions were identified, one for R = 3.60 Å, having an approximate 10% predicted contribution; however, this distance is 0.04 Å greater than the longest Cr-Fe(Cr) distance. The other path has R = 3.56 and a predicted amplitude of ~10%. Nevertheless, both paths are nonlinear (Fe→Fe→O→Fe or Fe→O→O→Fe) through O atoms. Although focused MS paths may be important in compounds with (near)linear, equidistant atomic arrangements, most MS paths involving nonlinear scattering through an O

Table 4. Effects of k window on the structural parameters obtained for FC10 (not cycled).

	Cr-O			Edge: Cr-Cr(Fe)			Corner: Cr-Cr(Fe)		
k	r(Å)	N	σ^2	r(Å)	N	σ^2	r(Å)	N	σ^2
3.6–13.9	2.00	5.91	0.006	3.04 3.24	2.72 2.20	0.005 0.005	3.47	3.30	0.009
3.3–10.8	2.01	5.73	0.006	3.04 3.24	2.46 2.40	0.005 0.005	3.49	3.56	0.009

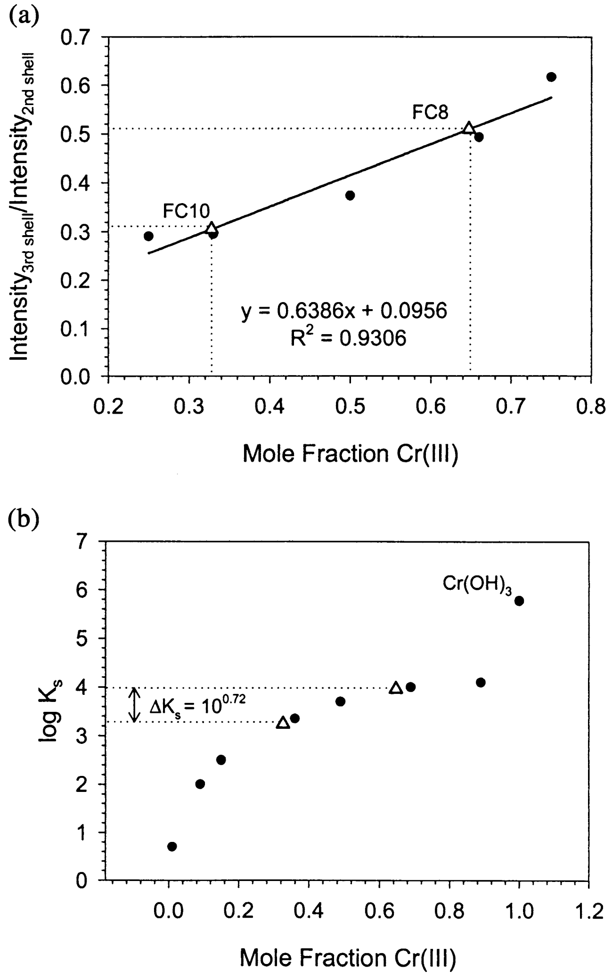

Fig. 9. (a) Correlation plot between mole fraction of Cr(III) in $Fe_{1-x}Cr_x(OH)_3 \cdot nH_2O$ and measured (circles) intensity of a corner-sharing peak at ~3.6Å (normalized to shortest Cr-Cr(Fe) contribution shell). FC8 (cycled) and FC10 (not cycled) are plotted (triangles) to determine the mole fraction of Cr(III) within the solid-phase products. (b) Solubility of $Fe_{1-x}Cr_x(OH)_3 \cdot nH_2O$ precipitates as a function of mole fraction of Cr(III) (circles) according to reaction 2 (Rai et al., 1986). Mole fraction for FC8 and FC10 (triangles) determined from (a) are included to estimate the relative solubility of the two solid-phase products.

atom contribute insignificant amplitude to the EXAFS spectra (O'Day et al., 1994). Additionally, the MS paths overlap with single-scattering paths at similar distances that have a greater amplitude contribution (R = 3.59, amplitude ratio = 24%). More importantly, inclusion of the MS paths does not significantly alter or improve the fit. We therefore conclude that multiple scattering does not contribute significantly to the spectra and that features within the third shell are primarily a result of single-scattering paths.

3.4. Solid-Phase Morphology

The morphology of secondary phase precipitates was investigated with scanning electron microscopy. Similar to α-FeOOH and/or β-FeOOH, solid-phase products display an acicular crystal habit (Fig. 10). Furthermore, the presence of twins (most likely, epitaxial) is evident giving rise to a starlike morphology within some solid-phase precipitates (Cornell and Schwertmann, 1996). The formation of twins occurs in high pH solutions or in the presence of α-Fe_2O_3 (Cornell and Giovanoli, 1985; Cornell and Schwertmann, 1996). However, epitaxial twins may also develop without the aforementioned conditions in the presence of ferrihydrite. Requirements for epitaxial twin development need only be a local hexagonal arrangement (a few unit cells) to permit growth in three different directions from the ordered region (Cornell and Giovanoli, 1985). Hence, twins within the solid-phase products may be induced by localized enhanced pH regions or, more likely, a consequence of nucleation on ferrihydrite.

4. CONCLUSIONS AND ENVIRONMENTAL IMPLICATIONS

Within Fe-reducing environments, the reduction of Cr(VI) by Fe(II) is kinetically favored. The reduction and immobilization of chromate is as a result of a coupled, biotic–abiotic reaction pathway, in which Fe(II) generated during iron respiration catalyzes the reduction of Cr(VI). The reduction pathway suggests that chromate reduction may be maintained on catalytic amounts of Fe as a result of the recycling of Fe within the system. Specifically, ferrous iron produced by iron-reducing bacteria will reduce Cr(VI) and subsequently (re)oxidize Fe(II) to Fe(III). Upon Cr(VI) reduction by aqueous Fe(II), the (re)oxidized Fe exists as a mixed Cr(III)-Fe(III) hydroxide phase. Iron-reducing bacteria may use this Cr(III)-Fe(III) hydroxide byproduct as a further metabolic substrate, thus regenerating Fe(II) reductant pools. Consequently, even in environments with only trace levels of iron, appreciable amounts of Cr(VI) could potentially be reduced.

As Fe is recycled, however, the hydroxide products become enriched in Cr relative to Fe approaching a pure $Cr(OH)_3 \cdot nH_2O$ phase. The solubility of $Fe_{1-x}Cr_x(OH)_3 \cdot nH_2O$ phases is a function of the mole fraction of Cr(III), represented by the following equation (Rai et al., 1986) (Fig. 9b):

$$\log K_s = 4.23 - 0.172(1 - x)^2 - 1.392(1 - x)^3 + \log x \tag{2}$$

The above reaction is based on a homogeneous solid solution, yet as mentioned earlier, the solids produced in this study are multidomainic and thus may demonstrate varying solubilities. Reaction 2, however, may provide a reasonable average solubility estimate for solely the Cr domains within the solid-phase products. As such, conversion from $Fe_{0.7}Cr_{0.3}(OH)_3 \cdot nH_2O$ to $Fe_{0.3}Cr_{0.7}(OH)_3 \cdot nH_2O$ results in an increase in solubility by an order of magnitude (Fig. 9b). For sustained reduction reactions, purification of Cr(III) within the solid may lead to a pure Cr phase, which is considerably more soluble than the Fe, Cr solid-solution phases (Rai et al., 1986; Sass and Rai, 1987). The enhanced solubility of Cr(III) hydroxide (γ) has been attributed to structural differences from the mixed Fe, Cr hydroxides (α/β) as was illustrated here and previously (Rai et al., 1986; Charlet and Manceau, 1992). Nevertheless, the overall solubility of Cr is substantially diminished through the initial reduction of Cr(VI) to the less soluble Cr(III) hydroxides.

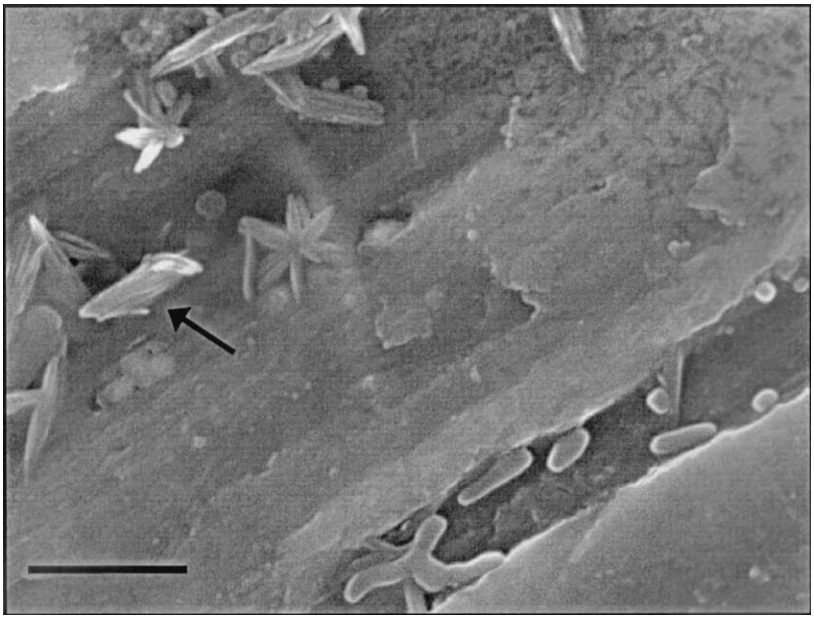

Fig. 10. Scanning electron micrograph (15 kV, WD = 18, 11,000×) of solid-phase products from biomineralization products in FC10 (not cycled). Secondary precipitates illustrate a lathelike crystal habit common to α/β-FeOOH (arrow). Multidomainic starlike α/β-FeOOH twins are also exemplified. Scale bar = 2 μm.

Acknowledgments—This research was funded by the Natural and Accelerated Bioremediation Research (NABIR) program, Biologic and Environmental Research (BER), U.S. Department of Energy (grant DE-FG03-00ER63029). We thank Professor Gordon Brown Jr., Tom Trainor, and Alexis Templeton for helpful suggestions, which greatly improved the manuscript. We also thank Ben Bostick for assistance in FEFF calculations and Stanford Synchrotron Radiation Laboratory for access to XAS facilities. We are also grateful to Dr. Don Sparks and three anonymous reviewers for their helpful comments and suggestions.

Associate editor: D. L. Sparks

REFERENCES

Balch W. E., Fox G. E., Magrum L. J., Woese C. R., and Wolfe R. S. (1979) Methanogens: Re-evaluation of a unique biological group. *Microb. Rev.* **43,** 260–296.

Bartlett R. J. and James B. (1979) Behavior of chromium in soils: III. *Oxidation. J. Environ. Qual.* **8,** 31–35.

Bianchi V. and Levis A. G. (1987) Recent advances in chromium genotoxicity. *Toxicol. Environ. Chem.* **15,** 1–24.

Caccavo F. Jr., Blakemore R. P., and Lovley D. R. (1992) A hydrogen-oxidizing, Fe(III)-reducing microorganism from the Great Bay Estuary, New Hampshire. *Appl. Environ. Microb.* **58,** 3211–3216.

Charlet L. and Manceau A. A. (1992) X-ray absorption spectroscopic study of the sorption of Cr(III) at the oxide–water interface. II. Adsorption, coprecipitation, and surface precipitation on hydrous ferric oxide. *J. Colloid Interface Sci.* **148,** 443–458.

Combes J. M., Manceau A., Calas G., and Bottero J. Y. (1989) Formation of ferric oxides from aqueous solutions: I. Hydrolysis and formation of ferric gels. *Geochim. Cosmochim. Acta* **53,** 583–594.

Combes J. M., Manceau A., and Calas G. (1990) Formation of ferric oxides from aqueous solutions: A polyhedral approach by X-ray absorption spectroscopy: II. Hematite formation from ferric gels. *Geochim. Cosmochim. Acta* **54,** 1083–1091.

Cornell R. M. (1988) The influence of some divalent cations on the transformation of ferrihydrite into more crystalline products. *Clay Mineral.* **23,** 329–332.

Cornell R. M. and Giovanoli R. (1985) Effect of solution conditions on the proportion and morphology of goethite formed from ferrihydrite. *Clays Clay Miner.* **33,** 424–432.

Cornell R. M. and Schwertmann U. (1996) *The Iron Oxides: Structure, Properties, Reactions, Occurrence and Uses.* VCH.

Eary L. E. and Rai D. (1989) Kinetics of chromate reduction by ferrous-ions derived from hematite and biotite at 25-degrees-C. *Am. J. Sci.* **289,** 180–213.

Fendorf S. E., Lamble G. M., Stapleton M. G., Kelley M. J., and Sparks D. L. (1994) Mechanisms of chromium(III) sorption on silica. 1. Cr(III) surface structure derived by extended X-ray absorption fine structure spectroscopy. *Environ. Sci. Technol.* **28,** 284–289.

Fendorf S. E. and Li G. (1996) Kinetics of chromate reduction by ferrous iron. *Environ. Sci. Technol.* **30,** 1614–1617.

Fendorf S., Wielinga B. W., and Hansel C. M. (2000) Chromium transformations in natural environments: The role of biological and abiological processes in chromium(VI) reduction. *Int. Geol.* **42,** 691–701.

Fischer W. R. and Schwertmann U. (1975) The formation of hematite from amorphous iron(III) hydroxide. *Clays Clay Miner.* **23,** 33–37.

Francis C. A., Obraztsova A. Y., and Tebo B. M. (2000) Dissimilatory metal reduction by the facultative anaerobe Pantoea agglomerans SP1. *Appl. Environ. Microb.* **66,** 543–548.

Fredrickson J. K., Kostandarithes H. M., Li S. W., Plymale A. E., and Daly M. J. (2000) Reduction of Fe(III), Cr(VI), U(VI), and Tc(VII) by Deinococcus radiodurans R1. *Appl. Environ. Microb.* **66,** 2006–2011.

George G. N. (1993) EXAFSPAK. Stanford Synchrotron Radiation Laboratory.

James B. R. and Bartlett R. J. (1983) Behavior of chromium in soils. 5. Fate of organically complexed Cr(III) added to soil. *J. Environ. Qual.* **12,** 169–172.

Kemner K. M., Kelly S. D., Orlandini K. A., Tsapin A. I., Goldfeld M. G., Perfiliev Y. D., and Nealson K. H. (2001) XAS investigations of Fe(VI). *J. Synch. Rad.* **8,** 949–951.

Lovley D. R. and Phillips E. J. P. (1994) Reduction of chromate by Dusulfovibrio vulgaris and its c_3 cytochrome. *Appl. Environ. Microb.* **60,** 726–728.

Lytle F. W., Greegor R. B., Sandstone D. R., Marques E. C., Wong J., Spiro C. L., Huffman G. P., and Huggins F. E. (1984) Measurements of soft x-ray absorption spectra with a fluorescent ion chamber. *Nucl. Instrum. Methods Phys. Res. Sect. A* **226,** 542–548.

Makos J. D. and Hrncir D. C. (1995) Chemistry of Cr(VI) in a constructed wetland. *Environ. Sci. Technol.* **29,** 2414–2419.

Manceau A. and Combes J. M. (1988) Structure of Mn and Fe oxides and oxyhydroxides: A topological approach by EXAFS. *Phys. Chem. Miner.* **15,** 283–295.

Manceau A. and Drits V. A. (1993) Local structure of ferrihydrite and feroxyhite by EXAFS spectroscopy. *Clay Miner.* **28,** 165–184.

National Research Council. (1974) *Medical and Biological Effects of Environmental Pollutants: Chromium.*National Academy of Science.

National Research Council. (1991) *Environmental Epidemiology*. National Academy Press.

O'Day P. A., Rehr J. J., Zabinsky S. I., and Brown G. E. Jr (1994) Extended X-ray absorption fine structure (EXAFS) analysis of disorder and multiple-scattering in complex crystalline solids. *J. Am. Chem. Soc.* **116,** 2938–2949.

Park C. H., Keyhan M., Wielinga B., Fendorf S., and Matin A. (2000) Purification to homogeneity and characterization of a novel Pseudomonas putida chromate reductase. *Appl. Environ. Microbiol.* **66,** 1788–1795.

Patterson R. R., Fendorf S., and Fendorf M. (1997) Reduction of hexavalent chromium by amorphous iron sulfide. *Environ. Sci. Technol.* **31,** 2039–2044.

Peterson M. L., Brown G. E. Jr., Parks G. A., and Stein C. L. (1997) Differential redox and sorption of Cr(III/VI) on natural silicates and oxide minerals: EXAFS and XANES results Geochim. *Cosmochim. Acta* **61,** 3399–3412.

Pettine M., Millero F. J., and Passino R. (1994) Reduction of chromium(VI) with hydrogen-sulfide in NaCl media. *Mar. Chem.* **46,** 335–344.

Pettine M., Dottone L., Campanella L., Millero F. J., and Passino R. (1998) The reduction of chromium(VI) by iron(II) in aqueous solutions Geochim. *Cosmochim. Acta* **62,** 1509–1519.

Rai D., Zachara J., Eary L., Girvin D. C., Moore C. A., Resch C. T., Sass B. M., Schmidt R. L. (1986) *Geochemical Behavior of Chromium Species.*Final report. Electric Power Research Institute.

Rehr J. J., de Leon J. M., Zabinsky S. I., and Albers R. C. (1991) Theoretical X-ray absorption fine-structure standards. *J. Am. Chem. Soc.* **113,** 5135–5140.

Rehr J. J., Albers R. C., and Zabinsky S. I. (1992) High-order multiple-scattering calculations of X-ray absorption fine structure. *Phys. Rev. Lett.* **69,** 3397–3400.

Ressler T., Wong J., Roos J., and Smith I. L. (2000) Quantitative speciation of Mn-bearing particulates emitted from autos burning (methylcyclopentadienyl)manganese tricarbonyl-added gasolines using XANES spectroscopy. *Environ. Sci. Technol.* **34,** 950–958.

Ryden J. C., Syers J. K., and Tillman R. W. (1987) Inorganic anion sorption and interactions with phosphate sorption by hydrous ferric-oxide gel. *J. Soil Sci.* **38,** 211–217.

Sass B. M. and Rai D. (1987) Solubility of amorphous chromium(III)-iron(III) hydroxide solid solutions. *Inorg. Chem.* **26,** 2228–2232.

Schwertmann U. and Murad E. (1983) Effect of pH on the formation of goethite and hematite from ferrihydrite. *Clays Clay Miner.* **31,** 277–284.

Schwertmann U. and Fechter H. (1994) The formation of green rust and its transformation to lepidocrocite. *Clay Miner.* **29,** 87–92.

Schwertmann U. Cornell R. M. (2000) *Iron Oxides in the Laboratory: Preparation and Characterization.* Wiley-VCH.

Sedlak D. L. and Chan P. G. (1997) The reduction of Cr(VI) by Fe(II) in natural waters Geochim. *Cosmochim. Acta* **61,** 2185–2192.

Stookey L. L. (1970) Ferrozine—A new spectrophotometric reagent for iron. *Anal. Chem.* **42,** 779–781.

Tebo B. M. and Obraztsova A. Y. (1998) Sulfate-reducing bacterium grows with Cr(VI), U(VI), Mn(IV), and Fe(III) as electron acceptors. *FEMS Microb. Let.* **162,** 193–198.

Urrutia M. M., Roden E. E., and Zachara J. M. (1999) Influence of aqueous and solid-phase Fe(II) complexants on microbial reduction of crystalline iron(III) oxides. *Environ. Sci. Technol.* **33,** 4022–4028.

Vermeul V. R., Gorby Y. S., Teel S. S., Al E. (1995) PNL-10633. Pacific Northwest Laboratory.

Vermeul V. R., Teel S. S., Amonette J. E., Cole C. R., Fruchter J. S., Gorby Y. A., Spane, Jr. F. A., Szecsody J. E., Williams M. D., and Yabusaki S. B. (1995) Geologic, Geochemical, Microbiologic, and Hydrologic Characterization at the In Situ Redox Manipulation Test Site. PNL-10633, Pacific Northwest National Laboratory Report.

Waychunas G. A., Apted M. J., and Brown G. E. Jr (1983) X-ray K-edge absorption spectra of Fe minerals and model compounds: Near-edge structure. *Phys. Chem. Minerals.* **10,** 1–9.

Wielinga B., Mizuba M. M., Hansel C. M., and Fendorf S. (2001) Iron promoted reduction of chromate by dissimilatory iron-reducing bacteria. *Environ. Sci. Technol.* **35,** 522–527.

Zachara J. M., Kukkadapu R. K., Fredrickson J. K., Gorby Y. A., and Smith S. C. (2002) Biomineralization of poorly crystalline Fe(III) oxides by dissimilatory metal reducing bacteria (DMRB). *Geomicrobiol. J.* **19,** 179–207.